Gamma Reaction History diagnostic determination of ablator areal density in NIF implosion experiments

C. Cerjan, D. B. Sayre, O. L. Landen, J. A. Church, W. Stoeffl, E. M. Grafil, H, W. Herrmann, N. M. Hoffman, Y. Kim

November 6, 2014

Physics of Plasmas

Disclaimer

This document was prepared as an account of work sponsored by an agency of the United States government. Neither the United States government nor Lawrence Livermore National Security, LLC, nor any of their employees makes any warranty, expressed or implied, or assumes any legal liability or responsibility for the accuracy, completeness, or usefulness of any information, apparatus, product, or process disclosed, or represents that its use would not infringe privately owned rights. Reference herein to any specific commercial product, process, or service by trade name, trademark, manufacturer, or otherwise does not necessarily constitute or imply its endorsement, recommendation, or favoring by the United States government or Lawrence Livermore National Security, LLC. The views and opinions of authors expressed herein do not necessarily state or reflect those of the United States government or Lawrence Livermore National Security, LLC, and shall not be used for advertising or product endorsement purposes.

Gamma Reaction History diagnostic determination of ablator areal density in NIF implosion experiments

C. Cerjan,[1, a] D. B. Sayre,[1] O. L. Landen,[1] J. A. Church,[1] W. Stoeffl,[1] E. M. Grafil,[2] H. W. Herrmann,[3] N. M. Hoffman,[3] and Y. Kim[3]

[1] *Lawrence Livermore National Labortory 7000 East Avenue, Livermore, CA 94550, USA*

[2] *Colorado School of Mines, Golden, Colorado, 80401, USA*

[3] *Los Alamos National Laboratory, Los Alamos, New Mexico, 87545, USA*

(Dated: 15 October 2014)

The inelastic neutron scattering induced γ-ray signal from ^{12}C in an ICF (Inertial Confinement Fusion) capsule is demonstrated to be an effective and general diagnostic for shell ablator areal density. Experimental detection of the time-integrated signal at 4.4 MeV using threshold detection from four gas Čerenkov cells provides a direct measurement of the ^{12}C areal density near stagnation. Data collected from a recent high neutron yield National Ignition Facility (NIF) campaign reveals two general trends: less remaining ablator mass at stagnation and higher shell density with increasing laser drive.

---

[a] Electronic mail: cerjan1@llnl.gov

A comprehensive characterization of the gas, fuel and ablator assembly is essential in the analysis of Inertial Confinement Fusion implosion experiments since attaining laboratory-scale ignition relies crucially upon symmetric convergence of a sufficiently dense fuel assembly. Although there are many implosion diagnostics currently fielded at the National Ignition Facility[1], these diagnostics generally rely upon x-ray emission to probe the hot core conditions thus providing only indirect information, derived from opacity variations, about the much colder fuel and remaining ablator assembly. Diagnostic approaches that rely upon nuclear processes are more amenable to this analysis, especially neutron scattering phenomena, since non-burning or non-emitting material may be probed. For example, the inelastic collisions of the DT-fusion neutrons with the compressed fuel and ablator induces an energy loss in the escaping neutrons that is cleanly monitored in the 10-12 MeV spectral range by the neutron Time-Of-Flight (nTOF) detectors. However, this process is dominated by the scattering from the dense deuterium-tritium (DT) layer and is thus much less sensitive to the remaining hydrocarbon ablator. An image of these scattered neutrons in the 6-12 MeV range is routinely available for higher yield implosions but, in addition to being more difficult to quantify, is still most sensitive to the DT layer.

The development of the Gamma Reaction History (GRH) diagnostic[2] complements these other approaches and provides a direct experimental determination of the areal density associated with the hydrocarbon ablator. Although the primary function of the GRH measurements is to provide a time history of the core fusion process by monitoring DT-γ emission, it is also possible to extract the bright 4.4-MeV γ rays from the $^{12}\text{C}(n, n'\gamma_{4.4})$ reaction. This γ-ray signal is unaffected by any of the competing scattering processes in the DT layer that complicate the interpretation of the nTOF-derived neutron spectra and neutron images. The calibrated time-integrated emission thus measures the spatially integrated hydrocarbon ablator areal density directly. Also, the nTOF spectra depend upon spatial variations in the shell density distribution along the line of sight between the burning core and the detector. Since the γ-ray emission is almost spatially isotropic, a single measurement inherently produces a shell-averaged areal density.

The significance of this data in characterizing implosion performance arises primarily from its implications for mixing of ablator mass into the dense DT fuel layer region. More specifically, if the remaining ablator mass is approximately constant in a series of nearly identical implosion experiments then an increase in the measured ablator areal density im-

2

plies entrainment of ablator material into the denser DT fuel layer. Since hydrodynamic instabilities are a dominant failure mechanism[3], trends in the hydrocarbon areal density might supply important information about the growth of these instabilities especially at the DT fuel-ablator interface.

An analysis of the recent series of high-yield implosion experiments conducted at the NIF provides an example of the utility of this approach[4]. With neutron yields in excess of 10^{15} signal detection in the GRH becomes statistically robust. Furthermore, the high-yield experimental campaign proceeded systematically in the sense that successive implosions varied by an increase in hohlraum drive. In the next section, the GRH experimental apparatus and data analysis will be described and in the third section, details of a simple model are provided that supplies a coherent framework in which to view the data. The presentation concludes with a brief discussion of the relevance of the analyzed data to the high-yield campaign and possible extensions of the GRH diagnostic.

I.   EXPERIMENTAL DETAILS AND DATA ACQUISTION

The GRH diagnostic consists of four gas cells with selectable pressures to adjust the Čerenkov threshold on Compton-scattered electrons in the active detector volume[5]. For the high-foot campaign the chosen thresholds correspond to γ-ray energies of 10, 8, 4.5 and 2.9 MeV. The 10 MeV and 8 MeV thresholds measure γ rays from the 4.2×10^{-5} branch of DT fusion[6]. Gamma rays produced from neutron interactions with materials surrounding the target dominate the 4.5 MeV threshold, while the 2.9 MeV signal divides somewhat evenly between $^{12}\text{C}(n, n'\gamma_{4.4})$ and the neutron-induced background.

Figure 1 shows a least squares fit which decomposes the 2.9 MeV data into a $^{12}\text{C}(n, n'\gamma_{4.4})$ signal and two backgrounds. Constraints were placed on each background. Measurement of an exploding pusher with negligible ablator and DT areal densities and the high-foot target holder determines the neutron-induced background for a given neutron yield. A $\leq 5\%$ contribution from the $\text{T}(d, \gamma)$ reaction was also taken into account. The $\text{T}(d, \gamma)$ yield, extracted from the two highest thresholds, combined with its γ-ray spectrum and the detector response determines the 2.9 MeV background. Calibration of the detector for $^{12}\text{C}(n, n'\gamma_{4.4})$ yield was performed in situ with an DT exploding pusher and a thin (1 cm) graphite disk a few inches from the exploding pusher to separate the carbon and
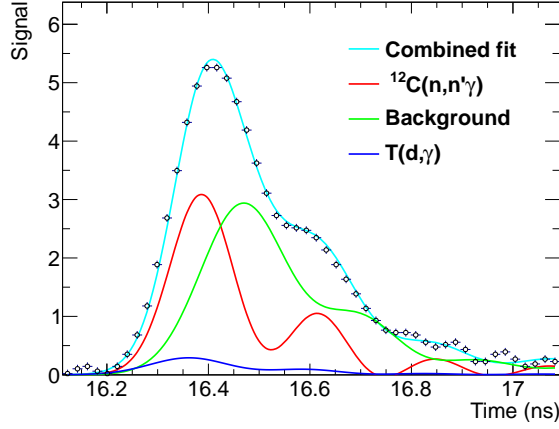
3

FIG. 1. A fit to the 2.9 MeV threshold data from a high-foot implosion, N140311. The data are an oscilloscope trace of the detector's signal over the burn duration. The curves result from convolving functions of γ-ray production with the impulse response function of the detector. A Gaussian source is assumed for the carbon signal. Note that signal ringing found in the fitted curves arises from the photomultiplier tube used in the detector.

fusion gamma signals in time. A conversion factor that transforms the time-integrated γ-ray signal from 2.9 MeV data into total number of ^{12}C$(n, n'\gamma_{4.4})$ reactions was determined from the calibration. The ^{12}C$(n, n'\gamma_{4.4})$ yield is determined by integrating the fitted signal and multiplying the result with the conversion factor. The ablator areal density depends on the ratio of 4.4 MeV γ rays to neutrons. While a calibration has been performed with a known ^{12}C areal density, its accuracy depends on similar neutron spectra between calibration shot and the measurement in question. For higher compression implosions, the DT areal density modifies the birth neutron spectrum by inelastic scattering processes, so this contribution requires a correction to the ^{12}C$(n, n'\gamma_{4.4})$ reactions at energies less than 14 MeV. Folding the downscattered spectrum with the ^{12}C$(n, n'\gamma_{4.4})$ cross section determines a correction of $\approx 20\%$ to the measured carbon ρR. Uncertainities from the downscatter correction and detector calibration limit the accuracy of the ρR measurements to $\pm 20\%$.

II. STATIC MODEL ANALYSIS

The high-yield campaign experiments retained the Si-doped hydrocarbon ablator as used in the National Ignition Campaign (NIC) but the laser drive was modified from four pulses to three with a higher energy first pulse ("high foot"). Physical estimates and radiation-hydrodynamic simulations suggested that this choice of laser drive would suppress fuel-ablator material mixing by reducing the compressibility of the DT fuel. This loss of compressibility decreases the likelihood of ignition since the necessary shell convergence cannot be attained, but increases the overall stability of the implosion[4]. The experimental consequence was that a ten-fold increase in neutron yield and very little ablator mix into the burning core were obtained with this experimental arrangement compared with the best-performing implosions during the NIC. Consistent with decreased compressibility, the fuel areal density declined by 30%. In addition to the laser drive alteration, three different initial ablator outer radii were investigated: a thicker shell matching that used in the NIC, 195 μm, and shells with 20 and 30 μm thinner radii. The variation in hydrocarbon shell thickness was selected to systematically increase the maximum implosion velocity without further increase in the laser drive power. Since these implosions produced higher neutron yield, there is interest in quantifying the implosion characteristics in detail.

Full three-dimensional hydrodynamical simulations of the high-yield campaign implosion series are computationally prohibitive, so a more tractable approach was selected to examine the experimental data trends. A validated three-dimensional static model used in earlier NIF campaigns was applied to the interpretation of the experimental data[7]. This model correlates the NIF implosion diagnostic information to deduce the thermodynamic properties of the burning core, the spatial density distribution of the DT fuel and the remaining hydrocarbon ablator in an attempt to generate a self-consistent description of the time-averaged implosion conditions. In essence, a three-dimensional volume is derived from the available x-ray and neutron images; assuming isobaric conditions at implosion stagnation, the hot core density and temperature variation are obtained; and the directional nuclear scattering and activation data is used to reconstruct the shell and ablator density distribution. The original DT fuel mass is also assumed to be conserved but the remaining hydrocarbon mass is of course variable. A representative image of the various fitting regions is plotted in Figure 2 for shot N120321. These fitting regions demarcate volumes of DT gas (region 1), the inner solid DT

fuel layer (region 2), the outer DT fuel layer (region 3), and the hydrocarbon layer (region 4). Regions 1, 2, and 3 are allowed to have variable hydrocarbon mix depending upon the specific details of an individual implosion.

Of particular interest in the work described here is the use of the time-integrated 4.4 MeV emission to fit the hydrocarbon areal density in the context of this model and thereby derive a better qualitative understanding of the stagnation conditions. It should be emphasized that the fitting procedure cannot provide a unique determination of the ablator areal density since independent measurements of the hydrocarbon density and its location are not available. The few constraints that exist arise from estimates of the remaining hydrocarbon ablator mass[8] and the ablator mass mixed into the burning core[9]. In the case of the high-yield series of implosions[4], very little ablator mix was observed in the burning core, implying that the remaining ablator material is either located in a compressed shell around the DT fuel assembly or entrained in the fuel assembly, or both. The ablator mass at stagnation is typically estimated from so-called "Convergent Ablator"implosions which rely upon x-ray back-lighting to measure capsule velocity and remaining mass. These implosions used the same laser drive conditions but replaced the DT ice layer with a comparable mass of hydrocarbon. Small corrections for residual differences in laser and capsule mass are included in the estimate of remaining mass for cryogenic DT layer implosions. As mentioned above, the cyrogenic implosions varied the laser energy, power, hohlraum lining material and ablator thickness to increase the incoming shell velocity which induced significant differences in the remaining mass and the GRH-derived ablator areal density.

Fits using the three-dimensional model to six of the high-yield implosions were performed: two of the thicker (N131119, N140511), two thinner (N140225, N140520) and thinnest (N140707) capsule configurations (see Table I). Additionally, one of the better-performing NIC implosion experiments, N120321, was included for comparison. The original static model was modified to replace the previous constant hydrocarbon ablator region with a quadratic exponentially decaying functional form[7]. As an example, density profiles in the fit to N140511 are plotted in Figure 3. An exponential form is physically reasonable since the hydrocarbon layer is releasing material without a boundary constraint after the shock passage that creates stagnation conditions while the quadratic decrease accounts for the spherical geometric contribution. Furthermore, the use of this simple fitting form provides some initial qualitative insight into the differences among the chosen implosions.
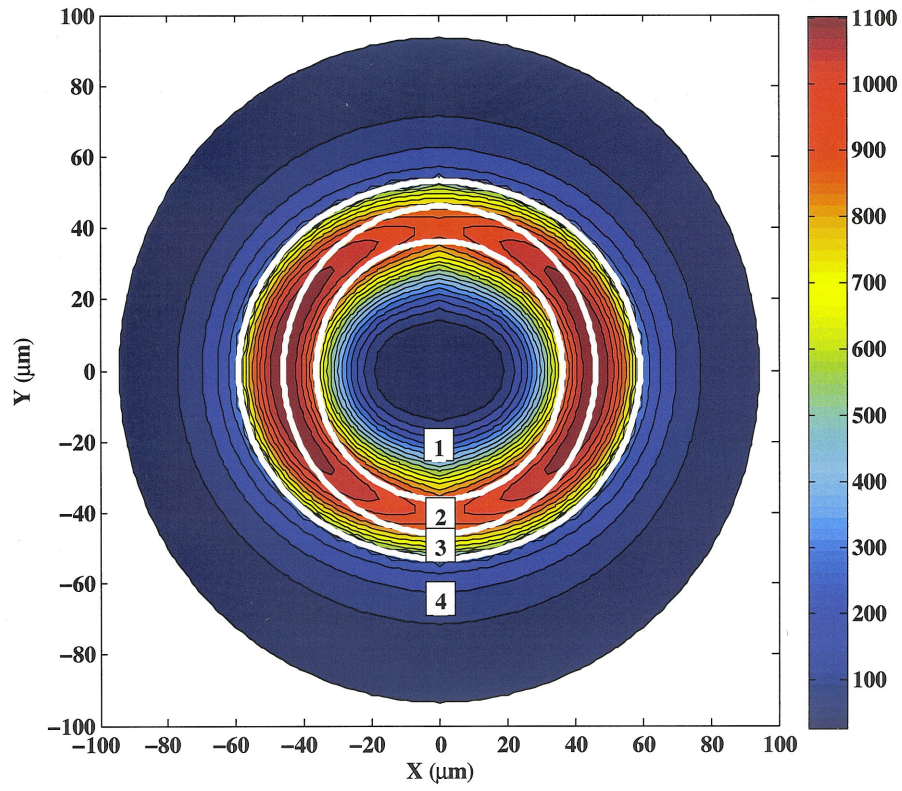
6

FIG. 2. Density contour plot of the three-dimensional static fit to N120321 with the separate material regions distinguished by the white line contours. Regions 1, 2 and 3 consist primarily of DT with possible admixtures of ablator material. Region 4 is pure hydrocarbon ablator material.
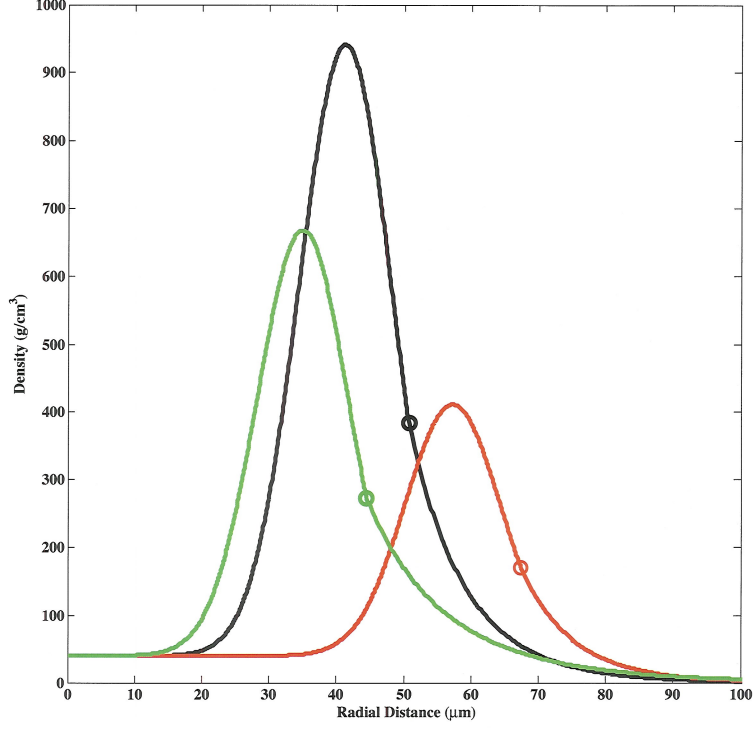
FIG. 3. Representative radial lineouts of the density distribution in the fit to N140511 using the decreasing quadratic and exponential decay fit to the remaining hydrocarbon ablator. The black, red and green curves refer to $\theta = 0$, $\pi/2$ and π radians respectively. The open circles indicate the matching radius of the fit along the angular ray.

Consider first, for simplicity, a spherical implosion assembly consisting of the DT gas and DT fuel layer, with the remaining hydrocarbon ablator matched to the exterior of the DT fuel layer. The DT regions are assumed to be uncontaminated by ablator material and the exterior ablator region is described by a linear exponential form decreasing quadratically

beyond a radius r_0 and matched to a Gaussian form that describes the DT fuel density

$$\rho(r) = \rho_{DT}(r_0)\left(\frac{r_0}{r}\right)^2 \exp[-\alpha(r-r_0)]\theta(r-r_0) \tag{1}$$

$$= \rho_0 \exp[-b(r_0-r_a)^2]\left(\frac{r_0}{r}\right)^2 \exp[-\alpha(r-r_0)]\Theta(r-r_0), \tag{2}$$

where r_0 is the matching radius and α is the inverse decay length. The ablator density at r_0 is required to match the compressed fuel Gaussian form which has a peak density of ρ_0, with a full width at half-maximum b, and radius at peak density of r_a. The Gaussian form is independently determined by fitting the x-ray and nuclear diagnostics, so the three parameters ρ_0,b,and r_a, are known. The remaining two parameters, α and r_0, will be determined using the GRH measured hydrocarbon areal density, ρ_{CH}, and the estimate of the remaining ablator mass, m_{CH}. The standard Heaviside step function, $\Theta(s)$, is zero for $s < 0$ and one for $s \geq 0$. The angle-averaged areal density constraint yields

$$\rho_{CH} = \frac{1}{4\pi}\int_0^{2\pi} d\varphi \int_0^{\pi} d\theta \sin\theta \int_0^{\infty} dr \, \rho(r)$$

$$= \rho_{DT}(r_0)r_0(1 + \alpha r_0 Ei(-\alpha r_0)), \tag{3}$$

where $Ei(x)$ is the exponential integral function. Applying the remaining mass constraint produces a simple relationship between the matching radius and inverse decay length

$$m_{CH} = \rho_{DT}(r_0)\int_0^{2\pi} d\varphi \int_0^{\pi} d\theta \sin\theta \int_0^{\infty} dr \, r_0^2 \, \theta(r-r_0)\exp[-\alpha(r-r_0)]$$

$$= 4\pi \frac{r_0^2}{\alpha}\rho_{DT}(r_0), \tag{4}$$

since m_{CH} is known experimentally. Replacing α in equation (2) produces an nonlinear equation for the remaining fit parameter, r_0. This nonlinear equation is readily solved by standard numerical techniques. A comparison of the selected implosion experiments is presented in Table I where the DT fuel layer parameters are assumed to be $r_a = 50\mu m$, $b = 10^6 cm^{-2}$, and $\rho_0 = 500g/cm^3$.

Even within the context of this oversimplified approach, conspicuous trends may be distinguished as a function of increasing implosion drive. For example, the lower velocity implosions, N131119, N140225, and N140707 have qualitatively similar matching densities and raii whereas the higher velocity implosion shots N140511 and N140520 display much higher matching densities and significantly reduced matching radii. Broadly speaking, the increased final velocity of these two latter shots, due to a combination of higher laser energy,

9

TABLE I. Experimental characteristics of the selected shots series including laser drive energy and hohlraum lining, capsule thickness, and peak implosion velocity. Peak densities, matching radii, and the e^{-1} ablator width (α^{-1}) are derived from a one-dimensional spherical exponential model using the experimental GRH hydrocarbon areal densities and remaining ablator mass. The corresponding averaged values from three-dimensional fitting are designated as $3D$. Error ranges for the experimental constraint values and the resultant fit quantities are indicated.

Shot	N120321	N131119	N140225	N140511	N140520	N140707
$Drive\ Energy\ (MJ)$	1.573 U(Au)	1.908 Au	1.568 Au	1.859 U(Au)	1.764 U(Au)	1.570 Au
$CH\ Thickness\ (\mu m)$	195	194	177	191	178	164
$Peak\ Velocity\ \left(\frac{\mu m}{ns}\right)$	321	352	333	372	389	350
$\rho r_{CH}\left(\frac{mg}{cm^2}\right)$	450 $\pm$90	229 $\pm$46	262 $\pm$52	295 $\pm$59	306 $\pm$61	197 $\pm$39
$m_{CH}\ (\mu g)$	319 $\pm$42	244 $\pm$41	279 $\pm$37	155 $\pm$40	140 $\pm$38	233 $\pm$34
$r_0\ (\mu m)$	53	58	57	53	51	59
$\rho_0\left(\frac{g}{cm^3}\right)$	263	96	109	281	358	76
$Width\ (\mu m)$	34	60	62	16	12	70
$3D\ r_0\ (\mu m)$	53 $\pm$5	57 $\pm$2	63 $\pm$3	54 $\pm$3	50 $\pm$5	65 $\pm$2
$3D\ \rho_0\left(\frac{g}{cm^3}\right)$	293 $\pm$108	99 $\pm$42	126 $\pm$54	328 $\pm$106	310 $\pm$75	86 $\pm$37
$3D\ Width\ (\mu m)$	27 $\pm$13	57 $\pm$19	43 $\pm$18	13 $\pm$7	15 $\pm$4	49 $\pm$21

higher albedo of the Au-lined uranium wall, and thinner shell, compressed a smaller amount of residual ablator mass to an approximate three-fold increase in density at a 10% reduced radius. There is a clear violation of this trend for the thinnest shell implosion, N140707. Since the remaining ablator mass is relatively large but with a small GRH-inferred areal density, the matching density is quite low at the large matching radius and the e^{-1} ablator width, α^{-1}, is large. These values suggest an significantly extended fuel and ablator assembly at stagnation.

In the three-dimensional fits to the selected implosions, more realistic conditions are introduced into the model. The density and radius at which the exponential model for the remaining ablator material begins is now a function of radial distance and spherical angle; hydrocarbon material may be introduced into the DT gas and fuel assembly; and other experimental constraints such as the burning core volume and fuel areal density are imposed.

More specifically, the previous fitting procedure is applied to determine the burning core and assembled DT fuel layer properties[7] but the fit is now extended to include the remaining mass and GRH-inferred ablator areal density values as constraints. Since the matching density and radius now depend upon the azimuthal and polar angles, the two constraint equations become

$$\rho_{CH} = \rho_{CH}\left(\theta_i, \varphi_j\right) \tag{5}$$

and

$$\frac{m_{CH}}{4\pi} = m_{CH}\left(\theta_i, \varphi_j\right) \tag{6}$$

at each angular mesh point (θ_i, φ_j). That is, the constraints are applied along each angular ray. Estimates of the error ranges of the fit quantities are obtained from combinations of the extreme limits of the experimental constraints.

It is perhaps easiest to visualize the results of the extended fitting procedure by comparing identical cross sectional views of the stagnated assembly. Figures 4-8 present this comparison in the equatorial plane for the analyzed implosion experiments in chronological order. Several clear trends may be noted. First, the better-performing low-adiabat implosion N120321 achieves the most favorable combination of high density mass distribution and relatively uniform assembly symmetry. The subsequent high-adiabat implosions do not attain this uniformly high density distribution. Second, all of the high-adiabat implosions appear to have cold fuel shape distortions and, in some cases, burning core asymmetries. Third, there are two implosions, N140511 and N140520, in which the peak hydrocarbon ablator layer density is several times larger than the peak densities in the other high-foot implosions. An examination of either the spherical or three-dimensional matching densities and the associated widths in Table I for these two shots reveals substantially higher matching densities and much shorter widths. According to this analysis, the ablator was thus very compressed conformally with the DT fuel layer. In all of the considered cases, though, the hydrocarbon ablator layer clearly remains outside the regions of highest DT fuel density corroborating the expected behavior of the high-adiabat design in this shot series.

A straightforward comparison to the spherical results may be obtained by a simple average of the angular matching densities and radii. These averaged values appear in Table I for the selected implosions. Despite the large angular asymmetries in the shell density distributions obtained for many of the implosions, the spherical model captures the qualitative
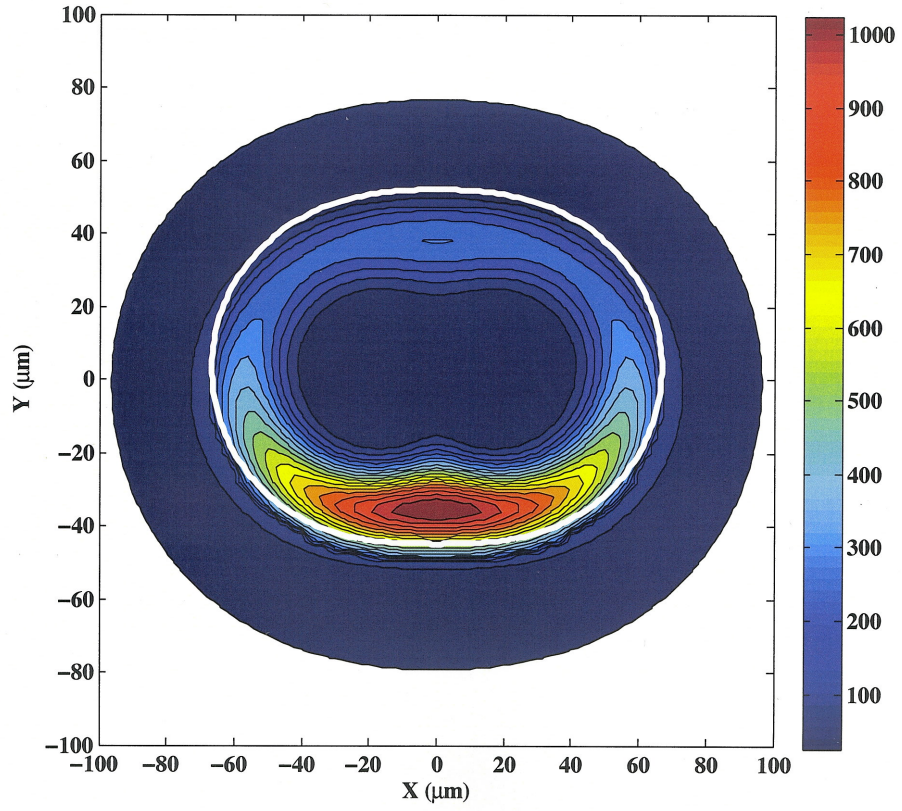
11

FIG. 4. Equatorial view of the density distribution obtained in the fit to shot N131119. The highlighted white contour marks the matching radius at which the hydrocarbon layer begins.
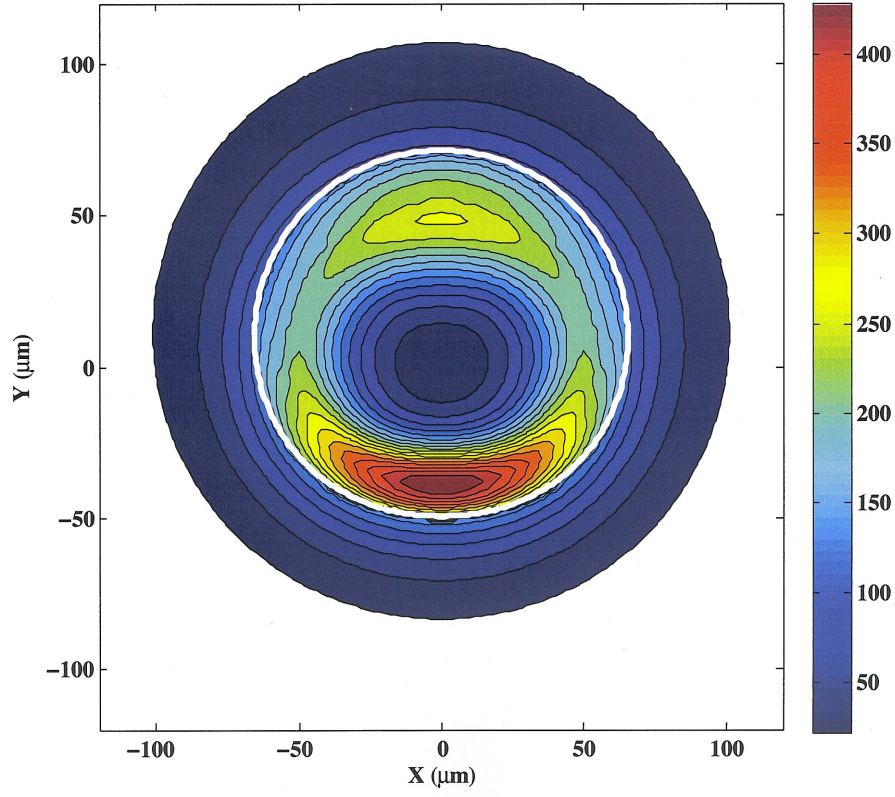
FIG. 5. Equatorial view of the density distribution obtained in the fit to shot N140225. The highlighted white contour marks the matching radius at which the hydrocarbon layer begins.
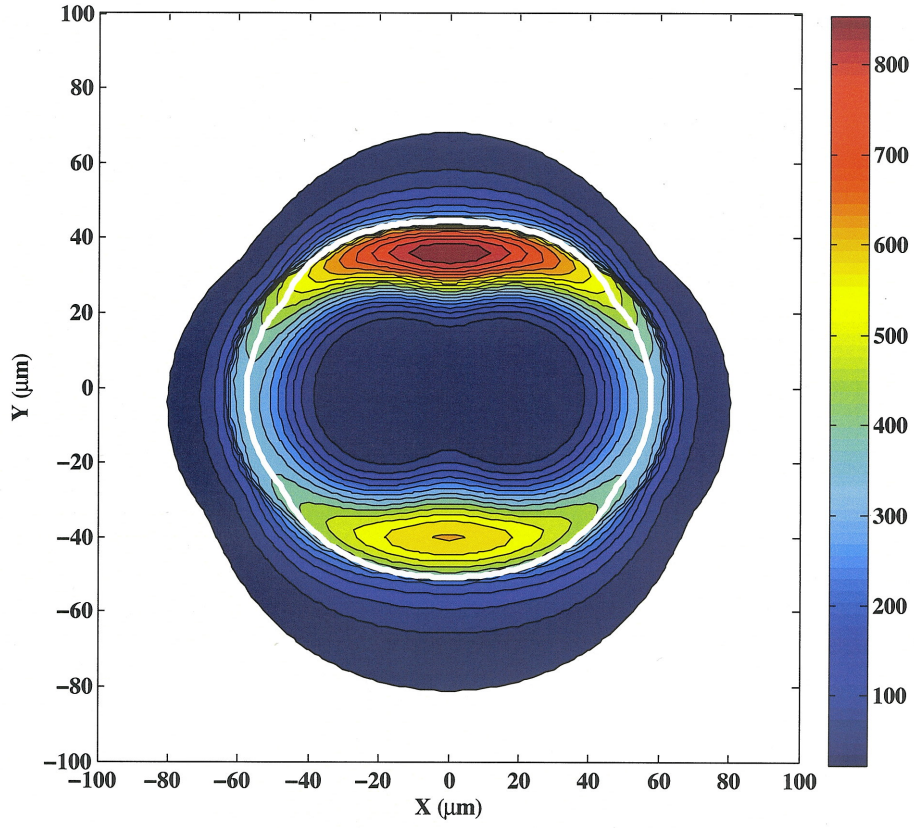
FIG. 6. Equatorial view of the density distribution obtained in the fit to shot N140511. The highlighted white contour marks the matching radius at which the hydrocarbon layer begins.
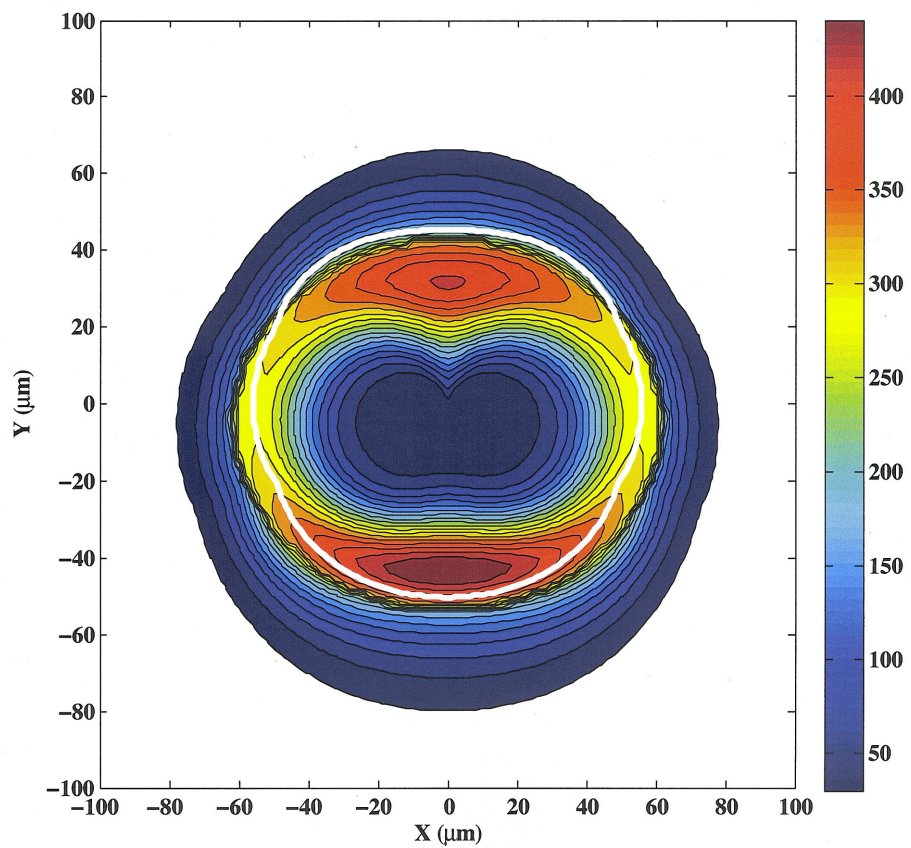
FIG. 7. Equatorial view of the density distribution obtained in the fit to shot N140520. The highlighted white contour marks the matching radius at which the hydrocarbon layer begins.
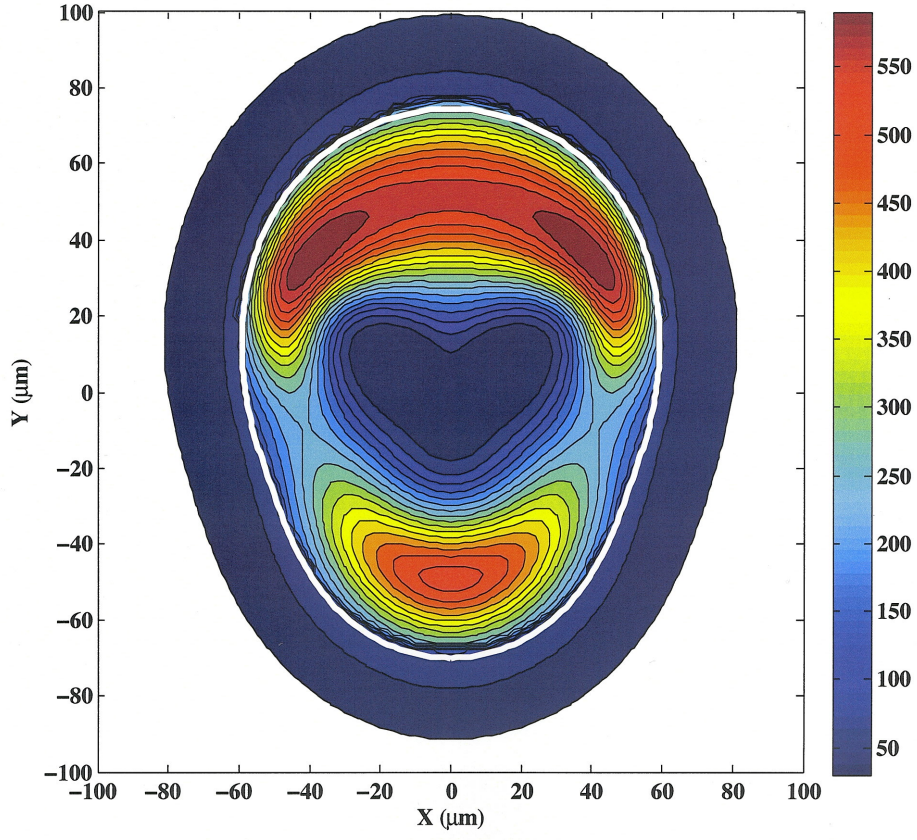
FIG. 8. Equatorial view of the density distribution obtained in the fit to shot N140707. The highlighted white contour marks the matching radius at which the hydrocarbon layer begins.

behavior of the compressed hydrocarbon ablator layer. For example, the matching radii are quite similar, with the exception of N140225 and N140707 which have quite uneven mass distributions. Furthermore, the trend of increasing matching density with increasing implosion velocity is generally reproduced in the high-foot series N131119 to N140520 but fails for N140707. The stagnation characteristics of the very thinnest shell implosion, N140707, are quite degraded compared to the other high-adiabat implosions but this difference likewise appears in both the spherical and full three-dimensional models. Despite this qualitative decrease in performance, very little ablator mix into the burning core is detected as measured by the standard x-ray yield diagnostic. The GRH results are thus in qualitative agreement with the expected experimental implosion design and also provide a quantitative measure of the relative difference in stagnation performance. Within the context of these simplified fitting techniques, the GRH-inferred ablator areal densities usefully complement the other stagnation diagnostic signatures and permit an extension of the three-dimensional static model to describe the time-averaged hydrocarbon density distribution at stagnation.

III.   CONCLUSION

The GRH diagnostic capability on the NIF is routinely used to obtain the temporal duration of neutron production in cyrogenic DT-layered implosions. The analysis above suggests that further valuable information about ignition-relevant implosions resides in the 4.4 MeV γ-ray signal. Some of the most important outstanding issues in the approach to achieving ignition concern the amount of DT fuel-ablator mix occuring and the overall compressibility of the assembled DT fuel and remaining ablator. As noted above, these issues might be directly diagnosed using the time-integrated 4.4 MeV γ-ray emission as captured by the GRH diagnostic. Furthermore, the spatial distribution of the remaining ablator density along specific lines of sight is necessary to model the high-energy x-ray self-emission of the burning core[9], since hydrocarbon and dopant opacity effects must be included in that analysis. The GRH signal will provide important constraints on those models. Finally, the 4.4 MeV GRH data complements the existing the Solid Radiochemical Collection (SRC) diagnostic fielded on the NIF[10]. In this diagnostic, activated Au hohlraum debris is collected and analyzed for the $(n, 2n)$ and (n, γ) products. The neutron capture product is especially sensitive to low-energy neutron production which is dominated by multiple scattering from

the remaining compressed ablator hydrogen. In principle, then, the SRC data measures the ablator hydrogen whereas the 4.4 MeV signal arises from the ablator ^{12}C. The synergy between these complementary measurements is being actively investigated for consistency and to enhance future radiochemical activation experiments on the NIF.

ACKNOWLEDGMENTS

REFERENCES

[1]M. J. Edwards, J. D. Lindl, B. K. Spears, S. V. Weber, L. J. Atherton, D. L. Bleuel, D. K. Bradley, D. A. Callahan, C. J. Cerjan, D. Clark, G. W. Collins, J. E. Fair, R. J. Fortner, S. H. Glenzer, S. W. Haan, B. A. Hammel, A. V. Hamza, S. P. Hatchett, N. Izumi, B. Jacoby, O. S. Jones, J. A. Koch, B. J. Kozioziemski, O. L. Landen, R. Lerche, B. M. MacGowan, A. J. MacKinnon, E. R. Mapoles, M. M. Marinak, M. Moran, E. I. Moses, D. H. Munro, D. H. Schneider, S. M. Sepke, D. A. Shaughnessy, P. T. Springer, R. Tommasini, L. Bernstein, W. Stoeffl, R. Betti, T. R. Boehly, T. C. Sangster, V. Yu. Glebov, P. W. McKenty, S. P. Regan, D. H. Edgell, J. P. Knauer, C. Stoeckl, D. R. Harding, S. Batha, G. Grim, H. W. Herrmann, G. Kryala, M. Wilke, D. C. Wilson, J. Frenje, R. Petrasso, K. Moreno, H. Huang, K. C. Chen, E. Giraldez, J. K. Kilkenny, M. Mauldin, N. Hein, M. Hoppe, A. Nikroo, and R. J. Leeper, Phys. Plasmas, **18**, 051003(2011).

[2]H. W. Herrmann, N. Hoffman, D. C. Wilson, W. Stoeffl, L. Dauffy, Y. H. Kim, A. McEvoy, C. S. Young, J. M. Mack, C. J. Horsfield, M. Rubery, E. K. Miller, and Z. A. Ali, Rev. Sci. Instrum. **81**, 10D333(2010); N. M. Hoffman, D. C. Wilson, H. W. Herrmann, and C. S. Young, Rev. Sci. Instrum. **81**, 10D332 (2010); N. M. Hoffman, H. W. Herrmann, Y. H. Kim, H. H. Hsu, C. J. Horsfield, M. S. Rubery, E. K. Miller, E. Grafil, W. Stoeffl, J. A. Church, C. S. Young, J. M. Mack, D. C. Wilson, J. R. Langenbrunner, S. C. Evans, T. J. Sedillo, V. Yu. Glebov, and T. Duffy, Phys. Plasmas **20**, 042705(2013).

[3]D. S. Clark, D. E. Hinkel, D. C. Eder, O. S. Jones, S. W. Haan, B. A. Hammel, M. M. Marinak, J. L. Milovich, H. F. Robey, L. J. Suter, and R. P. J. Town, Phys. Plasmas **20**,

056318(2013).

[4]T. R. Dittrich, O. A. Hurricane, D. A. Callahan, E. L. Dewald, T. Döppner, D. E. Hinkel, L. F. Berzak Hopkins, S. Le Pape, T. Ma, J. L. Milovich, J. C. Moreno, P. K. Patel, H.-S. Park, B. A. Remington, and J. D. Salmonson, Phys. Rev. Lett. **112**, 055002(2014); H.-S. Park, O. A. Hurricane, D. A. Callahan, D. T. Casey, E. L. Dewald, T. R. Dittrich, T. Döppner, D. E. Hinkel, L. F. Berzak Hopkins, S. Le Pape, T. Ma, P. K. Patel, B. A. Remington, H. F. Robey, and J. D. Salmonson, Phys. Rev. Lett. **112**, 055001(2014); O. A. Hurricane, D. A. Callahan, D. T. Casey, E. L. Dewald, T. R. Dittrich, T. Döppner, M. A. Barrios Garcia, D. E. Hinkel, L. F. Berzak Hopkins, P. Kervin, J. L. Kline, S. Le Pape, T. Ma, A. G. MacPhee, J. L. Milovich, J. Moody, A. E. Pak, P. K. Patel, H.-S. Park, B. A. Remington, H. F. Robey, J. D. Salmonson, P. T. Springer, R. Tommasini, L. R. Benedetti, J. A. Caggiano, P. Celliers, C. Cerjan, R. Dylla-Spears, D. Edgell, M. J. Edwards, D. Fittinghoff, G. P. Grim, N. Guler, N. Izumi, J. A. Frenje, M. Gatu Johnson, S. Haan, R. Hatarik, H. Herrmann, S. Khan, J. Knauer, B. J. Kozioziemski, A. L. Kritcher, G. Kyrala, S. A. Maclaren, F. E. Merrill, P. Michel, J. Ralph, J. S. Ross, J. R. Rygg, M. B. Schneider, B. K. Spears, K. Widmann, and C. B. Yeamans, Phys. Plasmas, **21**, 056314(2014).

[5]H. W. Herrmann, *et al.*, Journal of Physics:Conference Series **244**, 032047(2010).

[6]Y. Kim, J. M. Mack, H. W. Herrmann, C. S. Young, G. M. Hale, S. Caldwell, N. M. Hoffman, S. C. Evans, T. J. Sedillo, A. McEvoy, J. Langenbrunner, H. H. Hsu, M. A. Huff, S. Batha, C. J. Horsfield, M. S. Rubery, W. J. Garbett, W.Stoeffl, E. Grafil, L. Bernstein, J. A. Church, D. B. Sayre, M. J. Rosenberg, C. Waugh, H. G. Rinderknecht, M. Gatu Johnson, A. B. Zylstra, J. A. Frenje, D. T. Casey, R. D. Petrasso, E. Kirk Miller, V. Yu. Glebov, C. Stoeckl and T. C. Sangster, Phys. Rev. C**85**, 061601(2012).

[7]C. Cerjan, P. T. Springer, and S. M. Sepke, Phys. Plasmas **20**, 056319(2013).

[8]D. G. Hicks, N. B. Meezan, E. L. Dewald, A. J. Mackinnon, R. E. Olson, D. A. Callahan, T. Döppner, L. R. Benedetti, D. K. Bradley, P. M. Celliers, D. S. Clark, P. Di Nicola, S. N. Dixit, E. G. Dzenitis, J. E. Eggert, D. R. Farley, J. A. Frenje, S. M. Glenn, S. H. Glenzer, A. V. Hamza, R. F. Heeter, J. P. Holder, N. Izumi, D. H. Kalantar, S. F. Khan, J. L. Kline, J. J. Kroll, G. A. Kyrala, T. Ma, A. G. MacPhee, J. M. McNaney, J. D. Moody, M. J. Moran, B. R. Nathan, A. Nikroo, Y. P. Opachich, R. D. Petrasso, R. R. Prasad, J. E. Ralph, H. F. Robey, H. G. Rinderknecht, J. R. Rygg, J. D. Salmonson, M. B. Schneider, N. Simanovskaia, B. K. Spears, R. Tommasini, K. Widmann, A. B. Zylstra, G. W. Collins,

O. L. Landen, J. D. Kilkenny, W. W. Hsing, B. J. MacGowan, L. J. Atherton, and M. J. Edwards, Phys. Plasmas **19**, 122702(2012).

[9]T. Ma, P. K. Patel, P. T. Springer, M. H. Key, L. J. Atherton, L. R. Benedetti, D. K. Bradley, D. A. Callahan, P. M. Celliers, C. J. Cerjan, D. S. Clark, E. L. Dewald, S. N. Dixit, T. Döppner, D. H. Edgell, R. Epstein, S. Glenn, G. Grim, S. W. Haan, B. A. Hammel, D. Hicks, W. W. Hsing, O. S. Jones, S. F. Khan, J. D. Kilkenny, J. L. Kline, G. A. Kyrala, O. L. Landen, S. Le Pape, B. J. MacGowan, A. J. Mackinnon, A. G. MacPhee, N. B. Meezan, J. D. Moody, A. Pak, T. Parham, H.-S. Park, J. E. Ralph, S. P. Regan, B. A. Remington, H. F. Robey, J. S. Ross, B. K. Spears, V. Smalyuk, L. J. Suter, R. Tommasini, R. P. Town, S. V. Weber, J. D. Lindl, M. J. Edwards, S. H. Glenzer, and E. I. Moses, Phys. Rev. Lett. **111**, 085004(2013); S. P. Regan, R. Epstein, B. A. Hammel, L. J. Suter, J. Ralph, H. Scott, M. A. Barrios, D. K. Bradley, D. A. Callahan, C. Cerjan, G. W. Collins, S. N. Dixit, T. Doeppner, M. J. Edwards, D. R. Farley, S. Glenn, S. H. Glenzer, I. E. Golovkin, S. W. Haan, A. Hamza, D. G. Hicks, N. Izumi, J. D. Kilkenny, J. L. Kline, G. A. Kyrala, O. L. Landen, T. Ma, J. J. MacFarlane, R. C. Mancini, R. L. McCrory, N. B. Meezan, D. D. Meyerhofer, A. Nikroo, K. J. Peterson, T. C. Sangster, P. Springer, and R. P. J. Town, Phys. Plasmas, **19**, 056307(2012).

[10]J. M. Gostic, D. A. Shaughnessy, K. T. Moore, I. D. Hutcheon, P. M. Grant, and K. J. Moody, Rev. Sci. Instrum. **83**, 10D904(2012).